

Title	Coast/breakwater-integrated OWC: A theoretical model
Authors	Zheng, Siming;Zhang, Yongliang;Iglesias, Gregorio
Publication date	2019-04-15
Original Citation	Zheng, S., Zhang, Y. and Iglesias, G. (2019) 'Coast/breakwater-integrated OWC: A theoretical model', Marine Structures, 66, pp. 121-135. doi: 10.1016/j.marstruc.2019.04.001
Type of publication	Article (peer-reviewed)
Link to publisher's version	http://www.sciencedirect.com/science/article/pii/S0951833918304180 - 10.1016/j.marstruc.2019.04.001
Rights	© 2019 Elsevier Ltd. All rights reserved. This manuscript version is made available under the CC-BY-NC-ND 4.0 license - http://creativecommons.org/licenses/by-nc-nd/4.0/
Download date	2025-07-03 22:56:56
Item downloaded from	https://hdl.handle.net/10468/8379

1 **Title: Coast/breakwater-integrated OWC: a theoretical model**

2

3 Siming Zheng^a, Yongliang Zhang^b, Gregorio Iglesias^{a,c}

4

5 **Author names and affiliations:**

6 Siming Zheng

7 *E-mail address: siming.zheng@plymouth.ac.uk*

8

9 Yongliang Zhang

10 *E-mail address: yongliangzhang@tsinghua.edu.cn*

11

12 Gregorio Iglesias

13 *E-mail address: gregorio.iglesias@ucc.ie*

14

15 *a School of Engineering, University of Plymouth, Drake Circus, Plymouth PL4 8AA, United*
16 *Kingdom*

17 *b State Key Laboratory of Hydroscience and Engineering, Tsinghua University, Beijing,*
18 *100084, China*

19 *c Centre for Marine and Renewable Energy Ireland (MaREI), Environmental Research*
20 *Institute & School of Engineering, University College Cork, Ireland*

21

22

23

24 <https://doi.org/10.1016/j.marstruc.2019.04.001>

25 Received 19 October 2018; Received in revised form 3 January 2019; Accepted 6 April 2019

26 Available online 15 April 2019

27

28 **Abstract**

29 Integrating wave energy converters into coastal structures such as breakwaters, seawalls or jetties
30 not only offers benefits in terms of construction costs but also improves wave energy extraction.
31 In this paper a novel theoretical model based on linear potential flow theory is developed to study
32 the performance of an oscillating water column (OWC) integrated into a vertical structure in water
33 of finite water depth. The model has three fundamental advantages relative to previous works: no
34 thin-wall restriction (the thickness of the OWC chamber wall is considered), no singularities, and
35 far fewer truncating terms in the eigen-function expansions. The OWC chamber is a vertical
36 cylinder semi-embedded in the structure with a submerged, open bottom. As water waves impinge
37 on the structure, the water column in the chamber oscillates and drives an air turbine installed at
38 the chamber top to extract wave power. Using linear wave theory, the velocity potential in the
39 water domain is decomposed into scattering and radiation potentials whose unknown coefficients
40 are determined by the eigen-function matching method. Upon successful validation, the model is
41 used to investigate the influence of the thickness of the chamber wall and the radius and
42 submergence of the chamber on wave power absorption.

43

44 **Keywords:** Oscillating Water Column; Breakwater-integrated OWC; Wave energy; Potential flow;
45 Excitation volume flow; Hydrodynamic coefficients

46

47 1. Introduction

48 A large number of wave energy conversion concepts have been proposed since 1970s, which
49 can be roughly classified as: oscillating water column (OWC) (e.g., [1, 2]), point absorber (e.g.,
50 [3]), attenuator (e.g., [4]), oscillating wave surge converter (e.g., [5]), overtopping (e.g., [6]), and
51 others. Despite the large number of concepts proposed and investigated so far, only a few wave
52 energy converters (WECs) have been tested at a large scale, and even fewer have achieved the
53 fully commercial stage [7, 8]. The challenges in bringing WECs to the market include: high cost
54 of construction, installation and maintenance; negative environmental impact; poor reliability; and
55 low power extraction efficiency [9, 10]. It is not easy to solve all these problems concurrently
56 since some of them might be in conflict – and therein lie the challenges. For example, the
57 improvement of the reliability of WECs generally results in an increased cost of construction; to
58 enhance the power capture efficiency more sophisticated systems are typically necessary, but this
59 very sophistication is generally detrimental to the overall cost and survivability of the system.

60 The integration of a WEC into a marine structure, e.g., a breakwater, as opposed to its stand-alone
61 deployment in the open sea is an effective means to overcome a number of these challenges and
62 significantly increase the attractiveness of wave power exploitation [9, 11]. The integration not
63 only offers benefits in terms of shared costs of construction, but also improves the robustness of
64 the WEC and minimizes its environmental impact. Additionally, thanks to the wave power
65 absorbed by the WEC, wave reflection at the structure is diminished, which is often advantageous
66 from the points of view of coastal protection and non-interference with shipping. The synergies
67 between wave energy and marine structures have been investigated in a number of works, e.g.,
68 integration of an array of WECs with a breakwater [12], integration of an OWC into an offshore
69 wind turbine [13] or breakwater [14].

70 Among wave energy conversion technologies, OWC systems are especially simple, for the only

71 moving mechanical part is an air turbine/generator located above the water; therefore,
72 OWC-breakwater integration has received considerable attention [9]. Evans and Porter [15]
73 developed a theoretical model to simulate a two-dimensional (2D) OWC device composed of a
74 thin vertical surface-piercing barrier in front of a vertical wall. An integral equation for the
75 horizontal velocity across the gap under the thin barrier was adopted to deal with the singular
76 behaviour in the velocity field. Theoretical results showed that increasing the distance between the
77 barrier and the wall decreased the frequency at which resonance occurred. Later, Morris-Thomas,
78 Irvin [16] examined effect of the front barrier geometry on the performance of the OWC
79 experimentally. The hydrodynamic efficiency in short waves was found to decrease with the
80 increase of the barrier's submergence or thickness. More recently, the impact of the underwater
81 lips of an offshore OWC device in terms of both thickness and submergence was investigated by
82 Elhanafi, Fleming [17] with a two-dimensional computational fluid dynamics (CFD) model. By
83 selecting the optimal combination of the submergence and thickness of the lips, a peak efficiency
84 exceeding 0.79 was achieved, much larger than the 0.3 for a device with simpler, typical geometry.
85 Other aspects such as the role of the turbine Power Take-Off (PTO) system and the environmental
86 conditions in the power extraction of an onshore or bottom-fixed, breakwater-integrated OWC
87 have also been investigated. Sheng, Alcorn [18] proposed a numerical method based on potential
88 flow theory to assess the primary energy conversion of two generic OWC WECs (one bottom
89 fixed and another floating). The hydrodynamics and thermodynamics with consideration of the air
90 compressibility for different types of the air turbine PTOs (i.e., Wells turbine, impulse turbines and
91 bi-radial turbines) were coupled in the time-domain, and the numerical results appeared accurate
92 enough for the OWC power extraction assessment, especially for the bottom-fixed OWC. López
93 and Iglesias [19] developed a virtual laboratory based on artificial neural networks that can be
94 employed to obtain the pneumatic efficiency of a given OWC under specific wave condition, tidal
95 level and turbine damping. Physical model tests of these parameters were carried out as well [20].
96 In order to achieve an optimal energy transfer, Pereiras, López [21] described a methodology for
97 matching a nonlinear turbine to the OWC chamber. Elhanafi, Fleming [22] adopted a CFD model
98 to learn the impacts of both the PTO damping and incoming wave height on the performance of an
99 onshore OWC. The reflection coefficient and the energy absorption coefficient generally increase
100 and decrease with wave height. Research has also been directed towards other types of onshore or
101 bottom-fixed, breakwater-integrated OWCs, e.g., the U-type OWC [23, 24] and the multi-chamber
102 OWC [25]. Additionally, the integration of OWCs with floating breakwaters was considered by
103 He, Huang [26], He, Leng [27].

104 The above studies are focused on 2D problems of OWC-breakwater integration. In contrast,
105 there are few studies on its 3D aspects. For experimental work these require a wave basin rather
106 than a flume, with a scale model of the breakwater as well as the OWC itself [28]. For numerical
107 work, if the boundary element method is employed, the surfaces of the OWC device and the
108 surrounding breakwater or coastline must be divided into elements [29]; if the finite element
109 method is adopted, a numerical wave basin shall be established with the entire water volume
110 discretized [30]. Due to the considerable experimental and computational cost, 3D studies of
111 OWC-structure integration are not common. If the shapes of the structure and OWC are regular,
112 theoretical models may be used to solve the 3D hydrodynamic problem. Martins-rivas and Mei
113 [31] proposed a theoretical model based on the 3D wave radiation/diffraction theory and the usual
114 method of eigen-function expansions to study wave power extraction from an OWC at the tip of a

115 long and thin breakwater. The thin-walled OWC was represented by a hollow cylinder in their
116 model, in which the method for solving the integral equation of Evans and Porter [15] was used to
117 treat the singular behaviours in the velocity field beneath the thin wall of the OWC chamber. The
118 linearized air compressibility in the chamber was taken into account as part of the PTO system.
119 The effects of the radius and submergence of the OWC chamber, the air compressibility and the
120 incident wave direction were investigated. It was found that the free surface outside was strongly
121 dependent on the incident wave direction, whereas the power extracted was roughly insensitive to
122 the incident direction. Subsequently, Martins-rivas and Mei [32] applied the same theoretical
123 approach to a thin-walled OWC installed on a straight cliff-like coast. The performance of the
124 OWC was found to strongly depend on the incident wave direction. Wave reflection at the coast
125 could lead to up to a doubling in the power absorbed by the OWC. The role of either the radius or
126 submergence of the OWC was not considered. This theoretical model was later applied by Lovas,
127 Mei [33] to a vertical OWC at the tip of a general wedge-shaped coast.

128 In this context we propose a novel theoretical model based on linear potential flow theory to
129 evaluate the hydrodynamic performance and power extraction of the OWC. This novel approach
130 has three fundamental advantages relative to previous works. First, the thin-wall restriction is
131 removed, i.e., the thickness of the OWC chamber wall is taken into consideration. Second, there is
132 no singularity. Finally, far fewer truncating terms of the eigen-function expansions are required to
133 obtain accurate results. The effects of wall thickness, radius and submergence of the OWC on
134 power extraction can thus be investigated with the present model – as shown below.

135 The rest of the paper is organized as follows. Section 2 presents the relation between the PTO
136 system and the hydrodynamic problem. The basic governing equation, the boundary conditions for
137 wave scattering and radiation problems, and the expressions of the scattering and radiated velocity
138 potentials in different regions of the water domain are developed in Section 3, alongside the
139 method for solving the unknown coefficients. The expressions of excitation volume flow and
140 hydrodynamic coefficients are derived in Section 4. The model validation can be found in Section
141 5. The influence of the radius, wall thickness and submergence of the OWC chamber on wave
142 power absorption are investigated in Section 6. Finally, conclusions are drawn in Section 7.

143 2. Mathematical model

144 Consider an oscillating water column (OWC) installed on a vertical wall in a water domain of
145 uniform depth h (see Fig.1). The OWC chamber is composed of a vertical circular cylinder with a
146 ring shape cross section and it is half embedded in the wall. The outer and inner radii of the OWC
147 chamber are denoted as R and R_i , respectively. On the seaside, the chamber is open from a finite
148 submergence, denoted as d , to the seabed. As water waves propagate in the direction of β , the
149 water column enclosed by the OWC chamber oscillates and drives a Wells turbine (not plotted in
150 Fig. 1) installed at the chamber top to extract wave power.

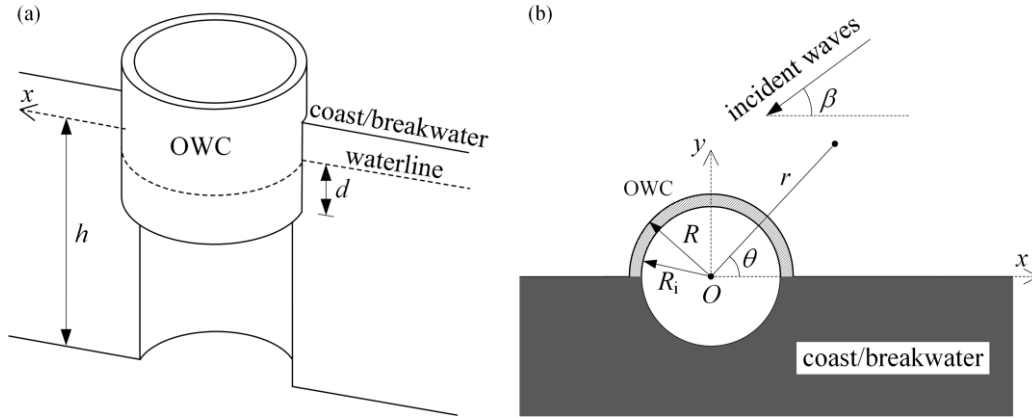


Fig. 1. Oscillating water column integrated into a coast/breakwater: (a) bird view; (b) top view.

As shown in Fig. 1, a general Cartesian coordinate system $Oxyz$ is adopted with the Oz axis at the location of the symmetrical vertical axis of the OWC pointing upward and the Ox axis along the waterline at the coast/breakwater. A polar coordinate $(Or\theta)$ is defined as given in Fig. 1b.

Subjected to regular waves of angular frequency ω with small amplitude, the flow problems may be treated in the linear potential theory regime in the frequency domain based on the assumption that the fluid is isotropic, incompressible inviscid, and the time-harmonic flow is irrotational. The fluid motion can be described by the velocity potential $\text{Re}[\Phi(r, \theta, z)e^{-i\omega t}]$, where Φ is a complex spatial velocity potential independent of time, t , and satisfies the Laplace equation, i represents imaginary unit. In a similar way, the air pressure inside the OWC chamber can be written as $\text{Re}(pe^{-i\omega t})$, where p is the complex air pressure amplitude inside the OWC chamber.

The spatial velocity potential Φ can be decomposed into the wave spatial potential, Φ_I , which represents the wave field when the vertical wall without OWC (i.e., a flat wall) is subjected to monochromatic incident waves, the diffracted wave spatial potential Φ_D induced by the existence of the OWC, and the radiated wave spatial potential as follows

$$\Phi = \Phi_I + \Phi_D + p\Phi_R, \quad (1)$$

where Φ_R is the spatial velocity potential due to unit air pressure oscillation inside the OWC chamber. Φ_I , Φ_D , and Φ_R all satisfy the Laplace equation, the boundary condition at the side wall of the coast/breakwater and the seabed boundary condition. Moreover, Φ_D and Φ_R must satisfy a radiation condition at infinite distance. Hereinafter, the sum of the incident and diffracted velocity potentials, which is the so-called scattering velocity potential (i.e., $\Phi_S = \Phi_I + \Phi_D$), is adopted for the sake of simplicity.

Considering the air turbine employed in the OWC is an idealized lossless linear Wells turbine and assuming the mass flux through the Wells turbines is proportional to the chamber air pressure, following Sarmento and Falcão [34] and Martins-rivas and Mei [32], the complex air pressure amplitude, p , is related to the scattering and radiated velocity potentials by:

$$\left[-i(a_{\text{PTO}} + a) + (c_{\text{PTO}} + c) \right] p = Q_e, \quad (2)$$

where a_{PTO} is used to take into account the effect of air compressibility, and can be expressed as $a_{\text{PTO}} = \omega V_0 / (v^2 \rho_0)$, in which V_0 is the air chamber volume, v denotes the sound velocity in air and ρ_0 represents the static air density; c_{PTO} is the damping of the PTO system depending on the

183 rotational speed of turbine blades, the scales of turbine rotor, the design of turbines and ρ_0 as well;
 184 Q_e , the so-called excitation volume flow, is the rate of upward displacement of the water surface
 185 inside the column contributed by the scattering potential:

$$186 \quad Q_e = \int_0^{2\pi} \int_0^{R_i} \frac{\partial \Phi_S}{\partial z} \Big|_{z=0} r dr d\theta, \quad (3)$$

187 c and a are hydrodynamic coefficients that can be derived from the volume flow inside the column
 188 induced by the radiated potential (i.e., Q_R),

$$189 \quad -(c - ia) = Q_R = \int_0^{2\pi} \int_0^{R_i} \frac{\partial \Phi_R}{\partial z} \Big|_{z=0} r dr d\theta. \quad (4)$$

190 The time-averaged power extraction by the PTO system (i.e., the Wells turbine), P , can be
 191 calculated by:

$$192 \quad P = \frac{c_{PTO}}{2} |p|^2 = \frac{c_{PTO}}{2} \frac{|Q_e|^2}{(c + c_{PTO})^2 + (a + a_{PTO})^2}. \quad (5)$$

193 The efficiency of wave power extraction is generally expressed by the relative wave capture
 194 width

$$195 \quad \eta = \frac{kP}{P_{in}} = \frac{2kP}{\rho g A^2 c_g}, \quad (6)$$

196 where P_{in} is the incident wave energy per unit width of the wave front; c_g is the group velocity of
 197 the incident wave.

198 Note that Q_e , c and a are fundamental for evaluating the performance of the OWC. In order to
 199 obtain these parameters, wave scattering and radiation problems, i.e., Φ_S and Φ_R , should be solved
 200 first.

201 3 Solution to scattering/radiated potentials

202 The governing equation and the boundary conditions for Φ_χ ($\chi=S, R$) can be written as follows:

$$203 \quad \frac{\partial \Phi_\chi}{\partial z} = 0, \quad z = -h, \quad (7)$$

$$204 \quad \frac{\partial \Phi_\chi}{\partial z} = 0, \quad R_i \leq r \leq R, \quad z = -d, \quad 0 < \theta < \pi, \quad (8)$$

$$205 \quad \frac{\partial \Phi_\chi}{\partial z} - \frac{\omega^2}{g} \Phi_\chi = 0, \quad r \geq R, \quad z = 0, \quad 0 < \theta < \pi, \quad (9)$$

$$206 \quad \frac{\partial \Phi_\chi}{\partial z} - \frac{\omega^2}{g} \Phi_\chi = \begin{cases} 0, & \chi = S \\ \frac{i\omega}{\rho g}, & \chi = R \end{cases}, \quad r \leq R_i, \quad z = 0, \quad 0 \leq \theta \leq 2\pi, \quad (10)$$

$$207 \quad \frac{\partial \Phi_\chi}{\partial \theta} = 0, \quad r > R, \quad -h \leq z \leq 0, \quad \theta = 0, \pi, \quad (11)$$

$$208 \quad \frac{\partial \Phi_\chi}{\partial \theta} = 0, \quad R_1 < r < R, \quad -h \leq z \leq -d, \quad \theta = 0, \pi, \quad (12)$$

$$209 \quad \frac{\partial \Phi_\chi}{\partial r} = 0, \quad r = R, \quad -d \leq z \leq 0, \quad 0 \leq \theta \leq \pi, \quad (13)$$

$$210 \quad \frac{\partial \Phi_\chi}{\partial r} = 0, \quad r = R_1, \quad -d \leq z \leq 0, \quad 0 \leq \theta \leq 2\pi, \quad (14)$$

$$211 \quad \frac{\partial \Phi_\chi}{\partial r} = 0, \quad r = R_1, \quad -h \leq z \leq -d, \quad \pi \leq \theta \leq 2\pi, \quad (15)$$

212 where ρ is the water density and g represents the gravity acceleration.

213 The entire fluid domain can be divided into three regions: I, inner region enclosed by the OWC,
 214 i.e., $r \leq R_1, 0 \leq \theta \leq 2\pi, -h \leq z \leq 0$; II, ring region beneath the OWC chamber, i.e., $R_1 \leq r \leq R, 0 \leq \theta \leq \pi, -h \leq z \leq -d$;
 215 III, outside region, i.e., $r \geq R, 0 \leq \theta \leq \pi, -h \leq z \leq 0$. Φ_χ ($\chi = S, R$) in these three regions are denoted as
 216 Φ_χ^{in} , Φ_χ^{ring} and Φ_χ^{out} , respectively.

217 3.1 Expressions of scattering/radiated potentials in different regions

218 In different regions, with the application of the method of separation of variables, Φ_χ ($\chi = S, R$)
 219 can be expressed by orthogonal series as follows [35, 36]:

220 I, inner region

$$221 \quad \Phi_\chi^{\text{in}}(r, \theta, z) = \sum_{m=-\infty}^{\infty} \sum_{l=0}^{\infty} \frac{\tilde{I}_m(k_l r)}{k_l \tilde{I}'_m(k_l R_1)} A_{m,l}^\chi Z_l(z) e^{im\theta} + \Phi_{p,\chi}^{\text{in}}, \quad (16)$$

222 where $A_{m,l}^\chi$ is the unknown coefficients to be determined; $\Phi_{p,\chi}^{\text{in}}$ is a particular solution,

$$223 \quad \Phi_{p,\chi}^{\text{in}} = \begin{cases} 0, & \chi = S \\ -\frac{i}{\rho\omega}, & \chi = R \end{cases} \quad (17)$$

$$224 \quad \tilde{I}_m(k_l r) = \begin{cases} J_m(k_l r), & l = 0 \\ I_m(k_l r), & l \neq 0 \end{cases} \quad (18)$$

225 in which J_m and I_m denote the Bessel function and the modified Bessel function of the first kind,
 226 respectively. k_0 is the wave number and k_l ($l > 0$) is the eigenvalue given by [37, 38],

$$227 \quad \omega^2 = -k_l g \tan(k_l h), \quad l = 1, 2, 3, \dots \quad (19)$$

228 $Z_0(z) = N_0^{-0.5} \cosh[k_0(z+h)]; Z_l(z) = N_l^{-0.5} \cos[k_l(z+h)];$ (20)

229 where

230 $N_0 = \frac{1}{2} \left[1 + \frac{\sinh(2k_0h)}{2k_0h} \right], N_l = \frac{1}{2} \left[1 + \frac{\sin(2k_lh)}{2k_lh} \right].$ (21)

231 II, ring region

232 $\Phi_\chi^{\text{ring}}(r, \theta, z) = \sum_{m=0}^{\infty} \left[F_{m,0}^\chi(r) + \sum_{l=1}^{\infty} \left(C_{m,l}^\chi \frac{I_m(\beta_l r)}{I_m(\beta_l R)} + D_{m,l}^\chi \frac{K_m(\beta_l r)}{K_m(\beta_l R)} \right) \cos[\beta_l(z+h)] \right] \cos m\theta,$
 233 (22)

234 where

235 $F_{m,0}^\chi(r) = \begin{cases} C_{m,0}^\chi + D_{m,0}^\chi \left[1 + \ln\left(\frac{r}{R}\right) \right], & m=0 \\ C_{m,0}^\chi \left(\frac{r}{R}\right)^{|m|} + D_{m,0}^\chi \left(\frac{r}{R}\right)^{-|m|}, & m \neq 0 \end{cases},$ (23)

236 in which $C_{m,l}^\chi$ and $D_{m,l}^\chi$ are the coefficients to be solved; K_m is the modified Bessel function of
 237 the second kind; β_l is the l -th eigenvalue which is given by

238 $\beta_l = \frac{l\pi}{h-d}, l=0, 1, 2, 3, \dots$ (24)

239 III, outside region

240 $\Phi_\chi^{\text{out}}(r, \theta, z) = \sum_{m=0}^{\infty} \sum_{l=0}^{\infty} E_{m,l}^\chi \frac{\tilde{K}_m(k_l r)}{\tilde{K}_m(k_l R)} \cos(m\theta) Z_l(z) + \Phi_{p,\chi}^{\text{out}},$ (25)

241 in which $E_{m,l}^\chi$ is the unknown coefficients to be determined; and $\Phi_{p,\chi}^{\text{out}}$ is a particular solution,

242 $\Phi_{p,\chi}^{\text{out}} = \begin{cases} \Phi_1, & \chi = \text{S} \\ 0, & \chi = \text{R} \end{cases},$ (26)

243 where, following Zheng and Zhang [37],

244 $\Phi_1(r, \theta, z) = -\frac{2igA}{\omega} \frac{Z_0(z)}{Z_0(0)} \sum_{m=0}^{\infty} \varepsilon_m (-i)^m J_m(k_0 r) \cos m\beta \cos m\theta,$ (27)

245 in which $\varepsilon_m=1$ for $m=0$, whereas $\varepsilon_m=2$ for $m \neq 0$.

246 $\tilde{K}_m(k_l r) = \begin{cases} H_m(k_l r), & l=0 \\ K_m(k_l r), & l \neq 0 \end{cases},$ (28)

247 where H_m denotes the Hankel function of the first kind.

248 3.2 Method of computation for unknown coefficients

249 The scattering and radiated spatial potentials as expressed in Sections 3.1 satisfy all the

250 boundary conditions shown in Eqs. (7) ~ (12) already. Additionally, the boundary conditions at
 251 $r=R$ and $r=R_i$, i.e., Eqs. (13)~(15), together with the pressure and velocity continuity conditions on
 252 the interfaces of two adjacent regions should be satisfied as well, which can be used to determine
 253 the unknown coefficients in Φ_χ . These continuity conditions for Φ_χ are given as follows:

254 1) Continuity of normal velocity at the boundary $r=R_i$:

$$255 \quad \frac{\partial \Phi_\chi^{\text{in}}}{\partial r} = \begin{cases} 0, & -d < z < 0, r = R_i, 0 \leq \theta \leq \pi; \text{ and } -h < z < 0, r = R_i, \pi \leq \theta \leq 2\pi \\ \frac{\partial \Phi_\chi^{\text{ring}}}{\partial r}, & -h < z < -d, r = R_i, 0 \leq \theta \leq \pi \end{cases} \quad (29)$$

256 2) Continuity of normal velocity at the boundary $r=R$:

$$257 \quad \frac{\partial \Phi_\chi^{\text{out}}}{\partial r} = \begin{cases} 0, & -d < z < 0, r = R, 0 \leq \theta \leq \pi \\ \frac{\partial \Phi_\chi^{\text{ring}}}{\partial r}, & -h < z < -d, r = R, 0 \leq \theta \leq \pi \end{cases} \quad (30)$$

258 3) Continuity of pressure at the boundary $r=R_i$:

$$259 \quad \Phi_\chi^{\text{ring}} = \Phi_\chi^{\text{in}}, \quad -h < z < -d, r = R_i, 0 \leq \theta \leq \pi \quad (31)$$

260 4) Continuity of pressure at the boundary $r=R$:

$$261 \quad \Phi_\chi^{\text{out}} = \Phi_\chi^{\text{ring}}, \quad -h < z < -d, r = R, 0 \leq \theta \leq \pi \quad (32)$$

262 After inserting the expressions of Φ_χ as given in Section 3.1 into these continuity conditions, i.e.,
 263 Eqs.(29)~(32), and making use of orthogonality of trigonometric functions and eigen-functions,
 264 the unknown coefficients in Φ_χ can be determined. For convenience, details of the derivations are
 265 given in Appendix A.

266 4 Excitation volume flow and hydrodynamic coefficients

267 4.1 Excitation volume flow

268 Once the unknown coefficients are determined, the excitation volume flow Q_e as given in Eq. (3)
 269 can be easily calculated by:

$$270 \quad Q_e = \frac{2\pi\omega^2 R_i}{g} \left(-\frac{A_{0,0}^D}{k_0^2} Z_0(z) + \sum_{l=1}^{\infty} \frac{A_{0,l}^D}{k_l^2} Z_l(0) \right). \quad (33)$$

271 4.2 Hydrodynamic coefficients

272 In a similar way, the hydrodynamic coefficients as given in Eq. (4) can be rewritten in terms of

273 $A_{m,l}^R$ as:

$$274 \quad -(c - ia) = Q_R = \frac{2\pi\omega^2 R_i}{g} \left(-\frac{A_{0,0}^R}{k_0^2} Z_0(z) + \sum_{l=1}^{\infty} \frac{A_{0,l}^R}{k_l^2} Z_l(0) \right). \quad (34)$$

275 The method, as shown in Eq. (4) or Eq. (34), which is derived from the radiated volume flow
 276 inside the column is a straightforward way for calculating the hydrodynamic coefficient, c .
 277 Actually there are two indirect methods as well for evaluating c , the one expressed by far-field
 278 coefficients as

279
$$c = 2\rho\omega h \sum_{m=0}^{\infty} \frac{1}{\varepsilon_m} \frac{|E_{m,0}^R|^2}{|H_m(k_0 R)|^2}, \quad (35)$$

280 which can be derived from Green's identity [36, 39]; and the other one derived from the excitation
281 volume flow Q_e based on Haskind Relation [32, 39]:

282
$$c = \frac{\omega Z_0(0)^2}{8\pi\rho g^2 h} \int_0^\pi |Q_e(\beta)|^2 d\beta. \quad (36)$$

283 The comparison of the results of c by using these two indirect methods as given in Eqs. (35) and
284 (36) with that of the direct method, i.e., Eq. (4) or Eq. (34), can be adopted as an approach to
285 validate the theoretical model.

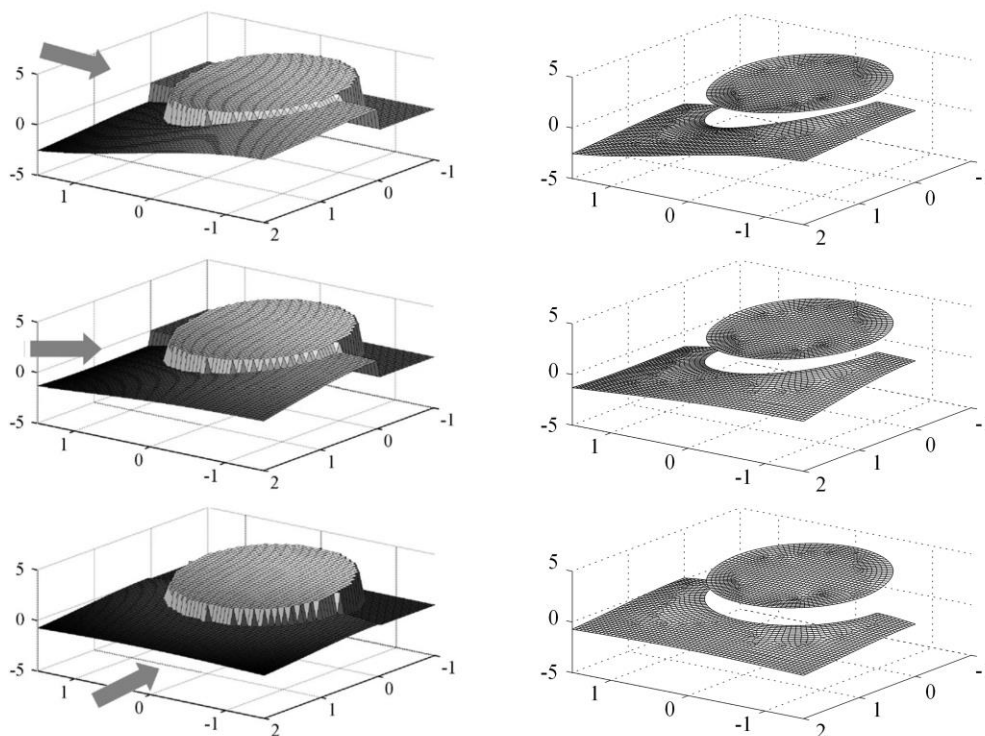
286 5 Model validation

287 Martins-rivas and Mei [32] solved the hydrodynamic problems from a thin-walled (i.e., $R_i=R$)
288 OWC along a straight coast for $R/h=0.5$, $d/h=0.2$ subjected to regular waves propagating at
289 different angles β with different values of kh . The present theoretical model without the thin-wall
290 restriction is adopted to re-simulate the same case, in which the inner radius is chosen as $R_i/h=0.49$,
291 i.e., $(R-R_i)/R=0.02$, to represent the thin chamber wall.

292 To make a comparison with the published results, the method as adopted in Martins-rivas and
293 Mei [32] for nondimensionalizing Q_e and hydrodynamic coefficients, c and a , i.e.,
294 $\bar{Q}_e = \omega Q_e / (ARg)$, $(\bar{c}, \bar{a}) = (c, a)\omega\rho/R$, is re-employed in the present section.

295 5.1 Wave scattering problem

296 The comparison between the present results of the free surface elevation pattern inside and
297 outside the OWC for $kh=1.64$ and those of Martins-rivas and Mei [32] is given in Fig. 2.



298

299 Fig. 2. Free surface elevation inside and outside the OWC for $R/h=0.5$, $d/h=0.2$, $kh=1.64$, $t=\pi/2\omega$.300 (left) results of Martins-rivas and Mei [32] for thin-walled OWC, i.e., $R_i=R$; (right) present results

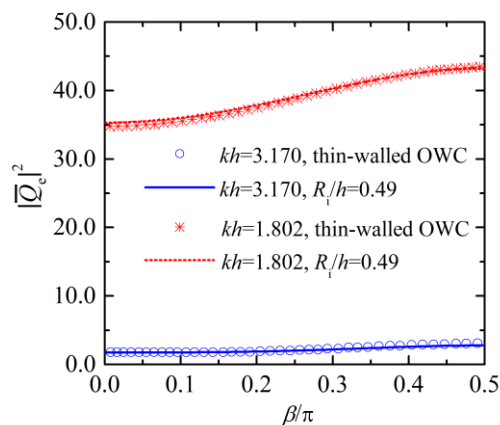
301

302 with $R_i/h=0.49$. The incidence angles $\beta=0, 0.25\pi, 0.5\pi$.

302

303 In addition, comparison of the excitation volume flow of the OWC as a function of incidence β 304 for $R/h=0.5$, $d/h=0.2$, $kh=3.170$ and 1.802 by using the present model with that of Martins-rivas

305 and Mei [32] is illustrated in Fig. 3.



306

307 Fig. 3. Excitation volume flow of the OWC as a function of incidence β for $R/h=0.5$, $d/h=0.2$.308 symbols: results from Martins-rivas and Mei [32] for thin-walled OWC, i.e., $R_i=R$; lines: present

309

310 results with $R_i/h=0.49$.

311 The excellent agreement of the present results with those of Martins-rivas and Mei [32], as

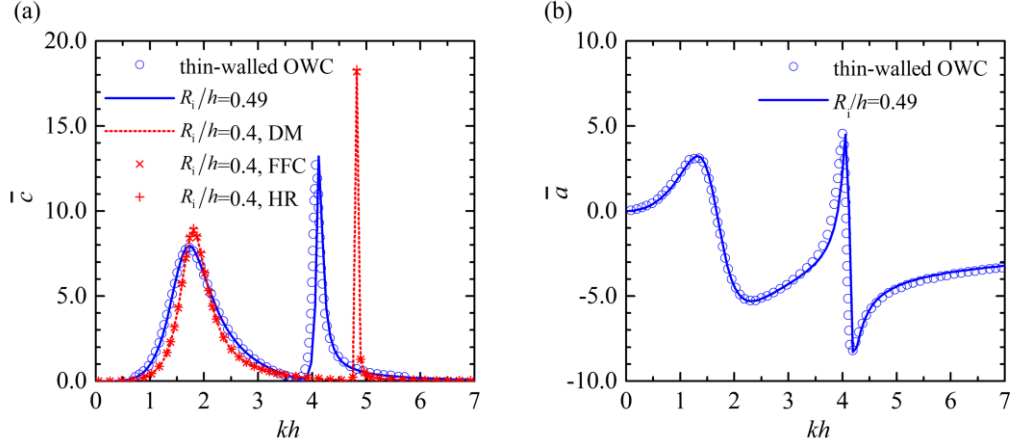
312 shown in Figs. 2 and 3, proves that the present theoretical model works pretty well in solving the

312

313 scattering problem.

313 5.2 Wave radiation problem

314 Figure 4 illustrates the frequency response of the hydrodynamic coefficients of the OWC with
 315 $R/h=0.5$, $d/h=0.2$. It can be learnt that the present results of c and a with $R_i/h=0.49$, i.e.,
 316 $(R-R_i)/R=0.02$, are in rather good agreement with those under thin-wall restriction [32]. What is
 317 more, results of c for the case with $R_i/h=0.4$ by using direct method (denoted as DM) and by
 318 adopting the other two indirect methods (denoted as FFC and HR, respectively) agree with each
 319 other pretty well, meaning the correctness of the present model in solving wave radiation problem.



320

321

322

323

324

325

326

327

328

329

Fig. 4. Frequency response of radiation damping and added mass of the OWC with $R/h=0.5$,
 $d/h=0.2$: (a) radiation damping; (b) added mass. Circles: results from Martins-rivas and Mei [32]
 for thin-walled OWC, i.e., $R_i=R$; lines and crosses: present results.

Note there is an obvious difference of the frequency response of radiation damping by using
 $R_i/h=0.4$ and $R_i/h=0.49$, reflecting the significant effect of the OWC chamber's thickness on the
 hydrodynamic characteristics of the OWC along a vertical wall. Influence of the thickness on the
 performance of the OWC deserves more attention and such effect will be discussed in the next
 section.

330 6 Results and discussion

331

332

Hereinafter, following Lovas, Mei [33], the dimensionless coefficients of Q_c and hydrodynamic
 coefficients, c and a , are redefined as follows:

333

$$\bar{Q}_c = \frac{\sqrt{g/h}}{Ahg} Q_c; \quad (\bar{c}, \bar{a}, \bar{c}_{PTO}, \bar{a}_{PTO}) = \frac{\rho\sqrt{g/h}}{h} (c, a, c_{PTO}, a_{PTO}), \quad (37)$$

334

with which, Eq. (6) can be rewritten as

335

$$\eta = \frac{khg}{c_g \sqrt{g/h}} \frac{\bar{c}_{PTO} |\bar{Q}_c|^2}{[(\bar{c} + \bar{c}_{PTO})^2 + (\bar{a} + \bar{a}_{PTO})^2]}. \quad (38)$$

336

337

338

Following Martins-rivas and Mei [32] and Lovas, Mei [33], a_{PTO} is calculated based on
 $\rho/\rho_0=1000$, $v=340$ m/s, $h=10$ m, and $V_0=\pi R^2 h$. The corresponding optimal PTO damping for a
 fixed OWC chamber (fixed V_0) is obtained by requiring $\partial P/\partial c_{PTO}=0$,

339

$$c_{PTO} = \sqrt{c^2 + (a + a_{PTO})^2}. \quad (39)$$

340

6.1 Comparison with an isolated offshore OWC and effect of incident wave direction

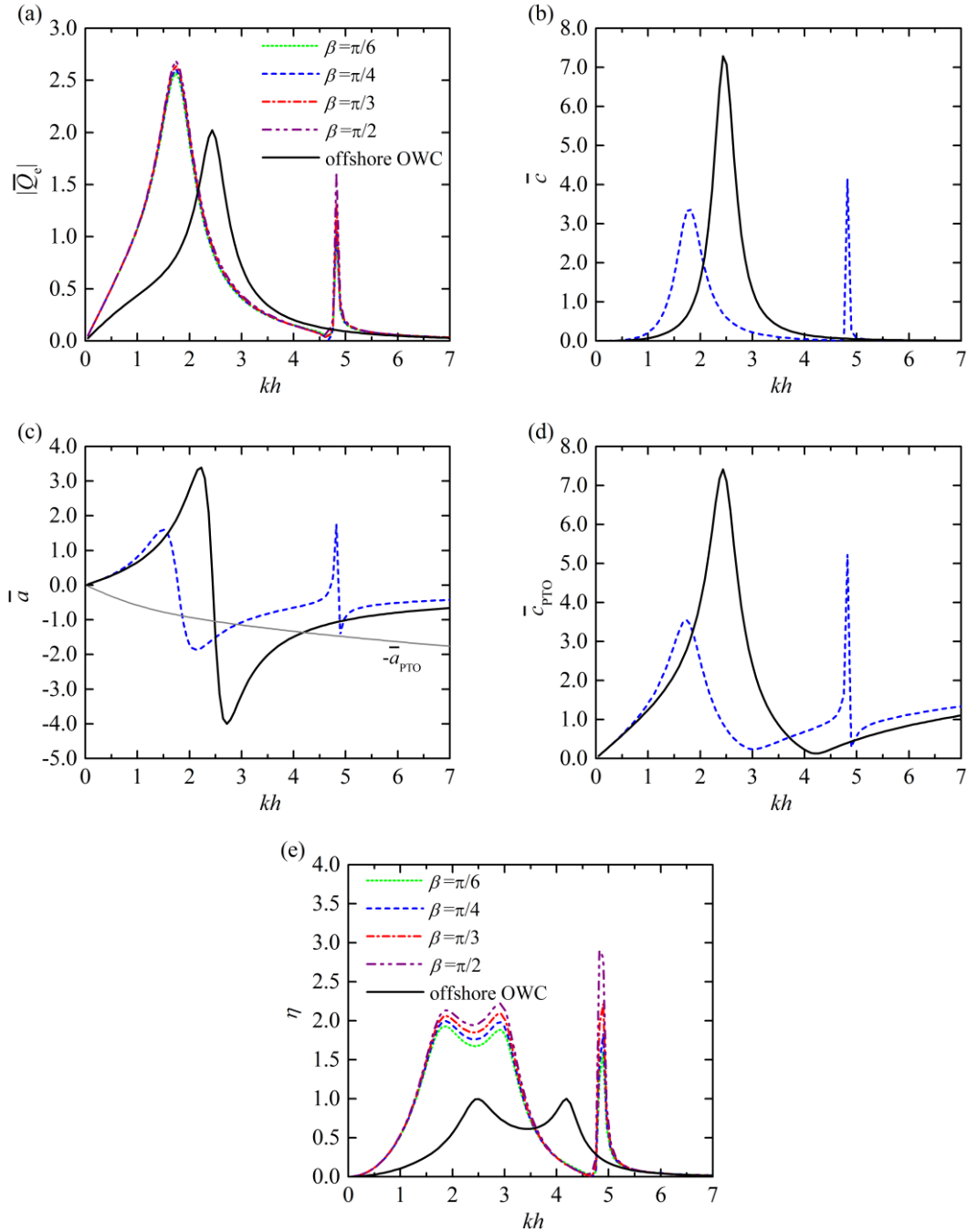
341 Figure 5 presents the frequency responses of wave excitation volume flux, hydrodynamic
 342 coefficients, turbine parameter and wave power capture factor when the coast/breakwater
 343 integrated OWC suffers from different incident directions. For reasons of symmetry, only the
 344 results for $\beta=\pi/6, \pi/4, \pi/3$ and $\pi/2$ are presented. For comparison, the results for the same OWC in
 345 the open sea are also displayed [36]. Only one blue dash curve as plotted in each figure of Figs.
 346 5b~5d is used to represent the results of \bar{c} , \bar{a} and \bar{c}_{PTO} for the coast/breakwater integrated
 347 OWC, respectively, since they are all independent of β .

348 For wave scattering problem of the isolated offshore OWC, in the computed range of kh , there
 349 is only one peak of $|\bar{Q}_e|-kh$ curve at $kh\approx 2.44$ (see Fig. 5a). Whereas for the coast/breakwater
 350 integrated OWC, apart from the main peak of $|\bar{Q}_e|-kh$ curve at $kh\approx 1.73$, a second sharp peak is
 351 also observed at a higher frequency, i.e., $kh\approx 4.82$. Such a feature can be identified from the view
 352 of natural modes in a closed cylinder in the radiation problem. For the isolated offshore OWC, the
 353 only peak of the $\bar{c}-kh$ curve occurs at $kh\approx 2.44$ (Fig. 5b), which corresponds to a piston-like
 354 motion, i.e., the so-called Helmholtz mode of oscillation. In a coast/breakwater integrated OWC,
 355 the Helmholtz mode cannot exist alone because of the asymmetry of the opening; another mode,
 356 i.e., the sloshing mode, is excited [32], and dominates the water motion inside the OWC chamber
 357 at $kh\approx 4.82$. As shown in Fig. 5c, the $\bar{a}-kh$ performs like a N letter shaped and a two-N letter
 358 shaped curves for an isolated offshore OWC and the integrated case, respectively, and the sign of
 359 \bar{a} changes rapidly at the kh where the peak of the $\bar{c}-kh$ curve occurs. These values of kh can be
 360 called the natural frequencies of the OWC in the absence of the PTO. The spiky behaviour of \bar{a}
 361 around these natural frequencies is connected to the peak of the $\bar{c}-kh$ curve. Note that the
 362 chamber coefficient ($-\bar{a}_{\text{PTO}}$) is also plotted in Fig. 5d as a gray solid curve, which intersects the
 363 $\bar{a}-kh$ curve at $kh\approx(2.48, 4.18)$ and $(1.86, 2.90, 4.90)$ for different cases. The kh -values where
 364 these intersections occur correspond the resonant frequencies of the OWC with the PTO system.
 365 For wave conditions corresponding to these resonant frequencies, \bar{a} and \bar{a}_{PTO} cancel each
 366 other, and it can be readily known from Eq. (2) that the air pressure inside the OWC chamber is in
 367 phase with the excitation volume flux. The frequency response of the optimal turbine parameter
 368 \bar{c}_{PTO} is illustrated in Fig. 5d, in which $\bar{c}_{\text{PTO}}=\bar{c}$ is satisfied at the resonant frequencies.

369 Compared with the single offshore OWC, the variation of \bar{c}_{PTO} for the coast/breakwater
 370 integrated OWC is less marked and less abrupt (except for $kh\approx 4.9$), which means that it may be
 371 easier to achieve in practice.

372 Finally, η as a function of kh for different values of the incident wave angle β is given in Fig. 5e.
 373 It is apparent that η for the isolated offshore OWC reaches the theoretical maximum value (i.e.,
 374 1.0) at these two resonant frequencies. Peaks of the $\eta-kh$ curve for the integrated case are also
 375 observed at the corresponding resonant frequencies. Thanks to the wave reflection from the
 376 coast/breakwater, the value of η for the coast/breakwater integrated OWC at $1.6<kh<3.1$ can be
 377 around twice as large as the theoretical maximum for the offshore case. Note that there is a

378 frequency between the second and the third resonant frequencies where no power can be
 379 extracted.



382
 383 Fig. 5. Comparison for different incident wave directions, β . (a) wave excitation volume flux
 384 $|\bar{Q}_e|$; (b) radiation damping \bar{c} ; (c) added mass \bar{a} and chamber coefficient $-\bar{a}_{PTO}$ (gray solid
 385 line); (d) turbine parameter \bar{c}_{PTO} ; (e) wave power capture factor η . In every case, $R/h=0.5$,
 386 $(R-R_i)/h=0.1$, $d/h=0.2$. Black solid line: isolated offshore OWC.

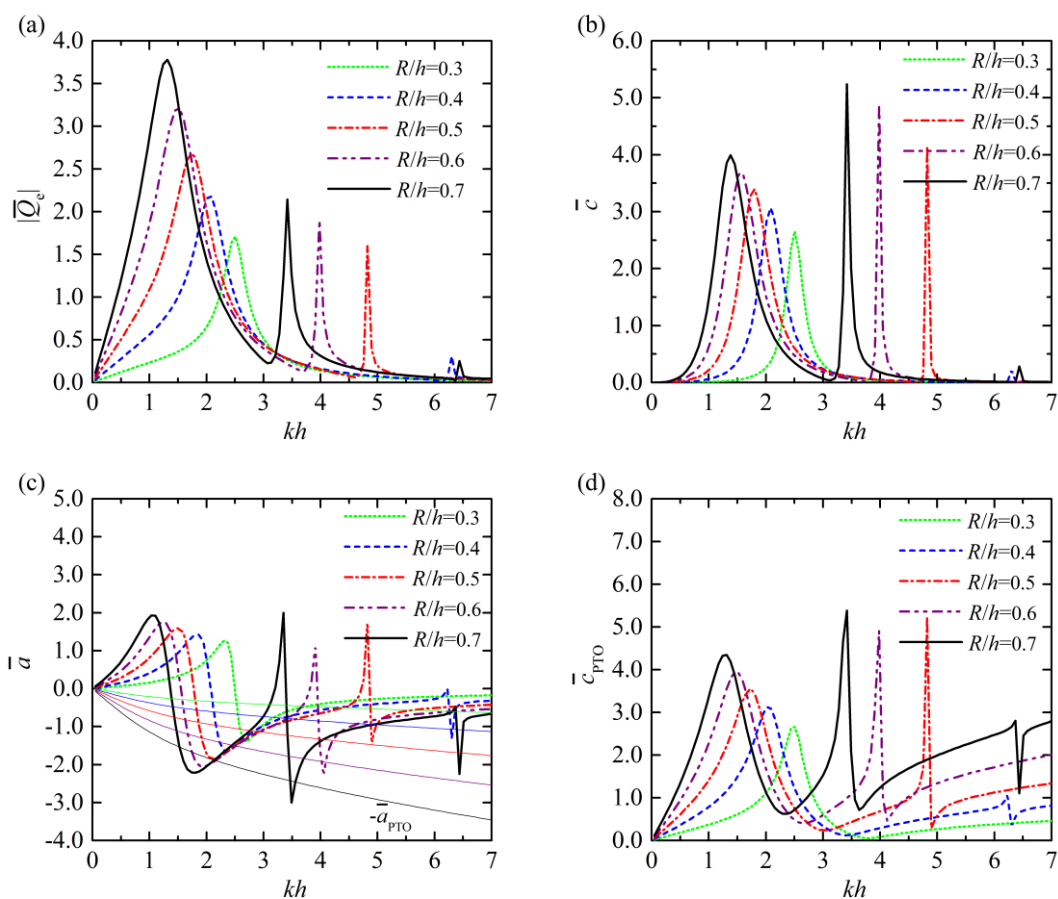
387 The effect of the incident wave direction β on $|\bar{Q}_e|$ is not obvious (Fig. 5a). As β increases
 388 from $\pi/6$ to $\pi/2$, this dependence is slightly visible at the natural frequencies. As a comparison, a

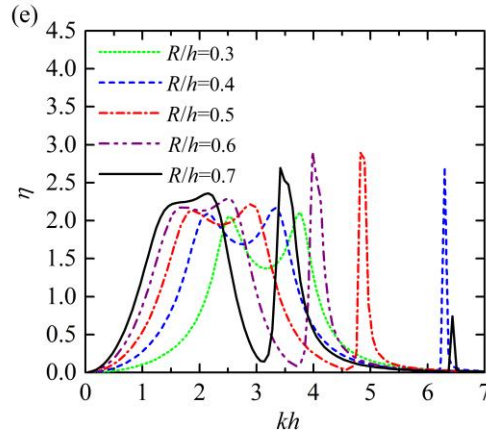
389 significant influence of β on η can be observed for $1.6 < kh < 3.1$ and $4.9 < kh < 5.0$ (Fig. 5e), where
 390 the more perpendicular the incident wave direction relative to the coast/breakwater, the more wave
 391 power that can be captured. Hereinafter, the effects of the other parameters will all be examined
 392 with $\beta = \pi/2$.

393 6.2 Radius of the OWC chamber

394 The coast/breakwater integrated OWCs with $R/h = 0.3 \sim 0.7$ are selected as five cases to
 395 investigate the effect of the radius of the chamber on the performance of the OWC (Fig. 6). As R/h
 396 increases, the highest peak of the $|\bar{Q}_c|$ - kh curve (Fig. 6a) shifts toward a lower frequency and
 397 gains intensity. Similar changes affect \bar{c} , \bar{a} and \bar{c}_{PTO} (Figs. 6b~6d). As R/h increases, more
 398 natural frequencies can be observed in the computed range of kh . For $R/h = 0.3$, there is only one
 399 natural frequency in the range of kh plotted, whereas for $R/h = 0.4, 0.5$ and 0.6 , there are two. For
 400 $R/h = 0.7$, three natural frequencies are readily observable.

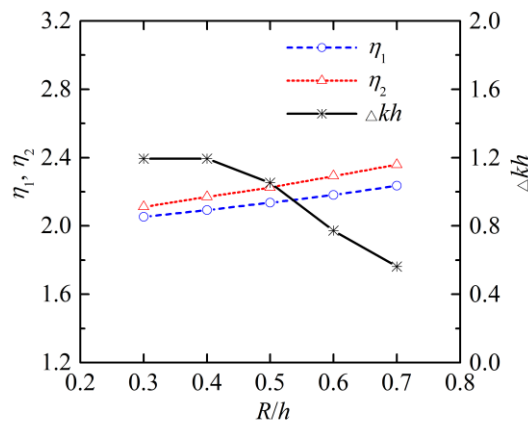
401





404 Fig. 6. Comparison for different radii of the OWC chamber, R/h . (a) wave excitation volume
 405 flux $|\bar{Q}_e|$; (b) radiation damping \bar{c} ; (c) added mass \bar{a} and chamber coefficient $-\bar{a}_{PTO}$ (thin
 406 solid lines, each of which corresponds to the line of \bar{a} plotted in the same color); (d) turbine
 407 parameter \bar{c}_{PTO} ; (e) wave power capture factor η . In every case, $(R-R_i)/h=0.1$, $d/h=0.2$, $\beta=\pi/2$.
 408

409 Given that the chamber volume V_0 ($V_0=\pi R^2h$) is dependent on R , there are also five $(-\bar{a}_{PTO})-kh$
 410 curves plotted in Fig. 6c corresponding to different values of R/h . For $R/h=0.3$, there are only two
 411 resonant frequencies in the computed range of kh . For the other cases, e.g., $R/h=0.6$, there could
 412 be four resonant frequencies in the same range of kh . As plotted in Fig. 6d, the larger the R/h , the
 413 higher and more abrupt the variation of \bar{c}_{PTO} . The plot of η (Fig. 6e) shows that when kh is
 414 between the first two resonant frequencies, as R/h increases, the $\eta-kh$ curve turns higher and flatter,
 415 and shifts toward lower frequencies. Here, Δkh is adopted to denote the difference between the
 416 first two resonant frequencies, and η_1 and η_2 are employed to represent the η -values corresponding
 417 to the first two resonant frequencies, respectively. Figure 7 presents η_1 , η_2 and Δkh as three
 418 functions of R/h . It is clear that, as R/h increases from 0.3 to 0.7, both η_1 and η_2 increase in a linear
 419 way approximately, whereas Δkh decreases dramatically from 1.19 to 0.56. Ideally the R/h ratio
 420 should be selected to achieve the balance between the peak value of η and its bandwidth, so that
 421 the OWC can capture the most power for a specified range of wave conditions.



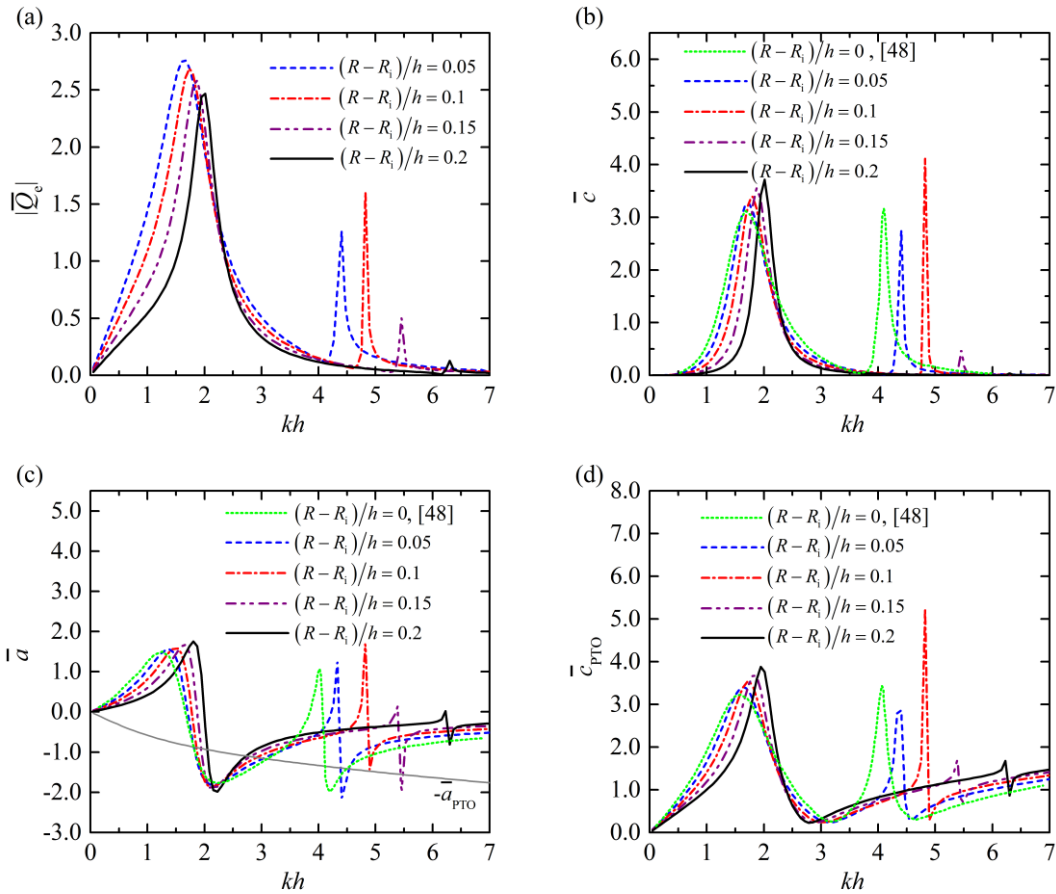
422
 423

Fig. 7. Variation of η_1 , η_2 and Δkh with R/h for $(R-R_i)/h=0.1$, $d/h=0.2$, $\beta=\pi/2$

424 6.3 Thickness of the OWC chamber

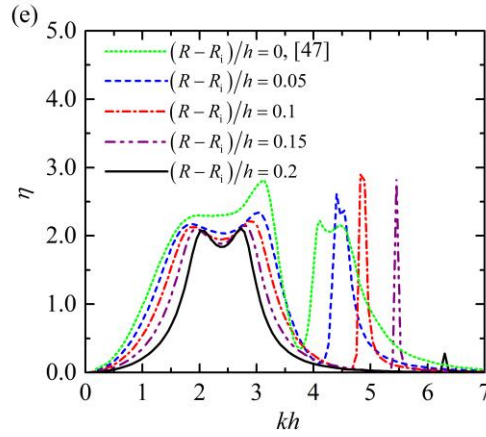
425 Figure 8 presents the results of the OWC chamber with $(R-R_i)/h=0.05, 0.1, 0.15$ and 0.2 , and the
 426 other parameters fixed at $R/h=0.5, d/h=0.2, \beta=\pi/2$. For comparison, some results of the thin-wall
 427 case, i.e., $(R-R_i)/h=0$, which were previously displayed by Martins-rivas and Mei [47] and Lovas
 428 et al. [48], are replotted in Fig. 8 as well. As $(R-R_i)/h$ increases, the inner radius of the chamber
 429 decreases, and the highest peak of $|\bar{Q}_c|$ - kh curve loses intensity and moves toward higher
 430 frequency as expected (see Fig. 8a). Meanwhile, the main peak of \bar{c} shifts toward higher
 431 frequency and turns higher and narrower. Similar changes are also found for \bar{a} and \bar{c}_{PTO} as
 432 given in Figs. 8c and 8d. It should be noted from Fig. 8c that with the increase of $(R-R_i)/h$, the first
 433 two intersection points of \bar{a} and $-\bar{a}_{PTO}$ get closer and closer to each other horizontally, hence
 434 the frequency band of η - kh as plotted in Fig. 8e turns narrower and narrower, whereas the
 435 frequency position of the middle of the band remains almost the same. In addition, the peaks of η
 436 corresponding to the first two resonant frequencies are lower as $(R-R_i)/h$ increases. Therefore,
 437 generally, the thickness of the OWC chamber should be as small as possible, so that larger and
 438 broader main peaks can be achieved and more wave power absorbed. Needless to say, the
 439 minimum thickness will be dictated in practice by structural considerations.

440



441

442



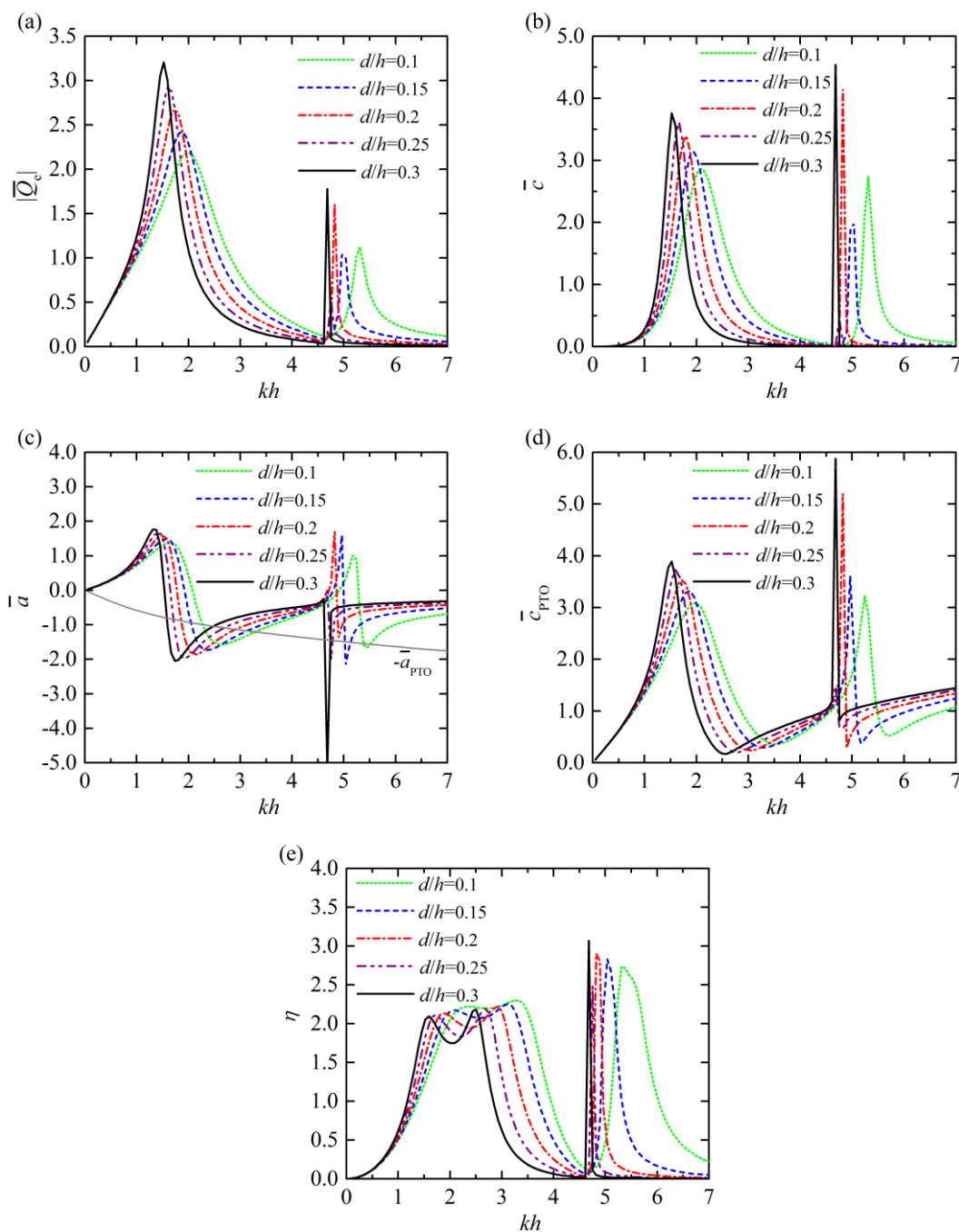
443
 444 Fig. 8. Comparison for different thicknesses of the OWC chamber wall, $(R-R_i)/h$. (a) wave
 445 excitation volume flux $|\bar{Q}_e|$; (b) radiation damping \bar{c} ; (c) added mass \bar{a} and chamber
 446 coefficient $-\bar{a}_{PTO}$ (gray solid line); (d) turbine parameter \bar{c}_{PTO} ; (e) wave power capture factor η .

447 In every case, $R/h=0.5$, $d/h=0.2$, $\beta=\pi/2$.

448 6.4 Submergence of the OWC chamber

449 Figure 9 compares the results for the coast/breakwater integrated OWC with different
 450 submergence of the chamber, i.e., $d/h = 0.1, 0.15, 0.2, 0.25$ and 0.3 , with $R/h=0.5$, $(R-R_i)/h=0.1$,
 451 $\beta=\pi/2$. The results of $|\bar{Q}_e|$ (Fig. 9a) show that with the increase of d/h , the highest peak of $|\bar{Q}_e|$
 452 turns higher and narrower, and shifts toward lower frequencies. Similar changes apply to \bar{c} and
 453 \bar{a} (Figs. 9b and 9c). This is reasonable, for the radiation loss becomes weaker. All the resonant
 454 frequencies in the computed range of kh reduce as d/h increases. The larger the d/h ratio, the
 455 higher and more abrupt the variation of the corresponding \bar{c}_{PTO} with kh (Fig. 9d), which may be
 456 more difficult to achieve in practice. The plot of η in Fig. 9e shows that, due to the change in the
 457 resonant frequencies, the peaks of η are shifted toward lower frequencies as well with the increase
 458 in d/h . Meanwhile, both η_1 and η_2 are found to decrease slightly, and the main bandwidth in terms
 459 of Δkh also decreases. The η corresponding to the kh between the first two resonant frequencies
 460 decreased more dramatically than η_1 and η_2 . It might be concluded that a better result can be
 461 obtained by using a smaller value of d/h .

462



463

464

465

466

467

468

469

470

471

472

Fig. 9. Comparison for different submergence of the OWC chamber, d/h . (a) wave excitation volume flux $|\bar{Q}_e|$; (b) radiation damping \bar{c} ; (c) added mass \bar{a} and chamber coefficient $-\bar{a}_{\text{PTO}}$

(gray solid line); (d) turbine parameter \bar{c}_{PTO} ; (e) wave power capture factor η . In every case,

$$R/h=0.5, (R-R_i)/h=0.1, \beta=\pi/2.$$

Note that d/h cannot be too small in practice, otherwise the opening might not be continuously submerged, especially when the OWC is subjected to incident waves with a large amplitude, to a large tidal range, or both.

473 7 Conclusions

474 In this paper a theoretical model based on linear potential flow theory is proposed to study the
 475 performance of an OWC along a vertical coast/breakwater without the thin-wall restriction of
 476 previous works. The water domain is divided into three regions, i.e., the interior region enclosed
 477 by the OWC chamber, the half-ring shaped region beneath the OWC chamber and the exterior
 478 region in front of the coast/breakwater extending towards infinite distance horizontally. Subjected
 479 to small amplitude incident regular waves, wave-structure interaction is decomposed into wave
 480 scattering and wave radiation problems. In order to determine the unknown coefficients of the
 481 scattering and radiated potentials in these three regions, the eigen-function matching method is
 482 employed. The wave power extraction of the OWC with linear PTO system is then evaluated in
 483 the frequency domain.

484 The influence of the vertical coast/breakwater is briefly discussed by comparing the
 485 performance of the integrated OWC with that of a similar isolated OWC deployed in the open sea.
 486 Finally, the effects of the radius, thickness and submergence of the chamber on the performance of
 487 the OWC along a coast/breakwater are investigated by means of the theoretical model. The
 488 following conclusions may be drawn.

489 The value of η for the coast/breakwater integrated OWC at specified ranges of kh can be around
 490 twice as large as the theoretical maximum of η for the offshore case due to the wave reflection
 491 from the coast/breakwater. The more perpendicular the incident wave direction relative to the
 492 coast/breakwater, the more wave power that can be captured by the OWC.

493 As the R/h ratio increases, more natural and resonant frequencies can be observed in the
 494 computed range of kh . The main peaks of η shift toward lower frequencies and the peak values
 495 increase nearly linearly with R/h , whereas the bandwidth reduces drastically.

496 The smaller the $(R-R_i)/h$ ratio, the larger and broader the main peaks of η , i.e., more wave power
 497 absorbed, and the frequency position of the middle of the band remains almost the same. Needless
 498 to say, an appropriate thickness, rather than zero thickness of the OWC chamber, will be dictated
 499 in practice by overall considerations, including not only wave power extraction but also structural
 500 survivability.

501 With the increase of d/h , the peaks of η are shifted toward lower frequencies. Meanwhile, both
 502 η_1 and η_2 are found to decrease slightly, and the main bandwidth in terms of Δkh is reduced.

503 To capture wave power on a large scale, it is expected that multiple OWCs along a
 504 coast/breakwater will be required. It is possible to extend the present theoretical model to multiple
 505 OWCs, as will be reported elsewhere.

506

507 Acknowledgements

508 The research was supported by National Natural Science Foundation of China (51679124,
 509 51479092) and Intelligent Community Energy (ICE), INTERREG V FCE, European Commission
 510 (Contract No. 5025).

511 Appendix A. Integral equations of the scattering and radiation problems

512 After inserting Eqs. (16) and (22) into Eq.(29), multiplying both sides by $Z_\zeta(z)e^{-i\tau\theta}$ and
 513 integrating for $z \in [-h, 0]$ and $\theta \in [0, 2\pi]$, for any pair of integer (τ, ζ) , it can be obtained that

$$514 \quad 2\pi h A_{\tau,\zeta}^{\chi} = \sum_{l=0}^{\infty} \left[\frac{\pi}{\varepsilon_{|\tau|}} \left(X_{|\tau|,l}^{(1)} C_{|\tau|,l}^{\chi} + Y_{|\tau|,l}^{(1)} D_{|\tau|,l}^{\chi} \right) + i \sum_{\substack{m=0 \\ m \neq |\tau|}}^{\infty} \frac{\tau \left[(-1)^{\tau-m} - 1 \right]}{\tau^2 - m^2} \left(X_{m,l}^{(1)} C_{m,l}^{\chi} + Y_{m,l}^{(1)} D_{m,l}^{\chi} \right) \right] L_{l,\zeta},$$

$$515 \quad (A.1)$$

516 where

$$517 \quad X_{\tau,\zeta}^{(1)} = \begin{cases} \frac{\tau}{R} \left(\frac{R_1}{R} \right)^{\tau-1}, & \zeta = 0 \\ \frac{\beta_{\zeta} I'_{\tau}(\beta_{\zeta} R_1)}{I_{\tau}(\beta_{\zeta} R)}, & \zeta \neq 0 \end{cases}; \quad Y_{\tau,\zeta}^{(1)} = \begin{cases} \frac{1}{R_1}, & \zeta = 0, \tau = 0 \\ -\frac{\tau}{R} \left(\frac{R}{R_1} \right)^{\tau+1}, & \zeta = 0, \tau \neq 0. \\ \frac{\beta_{\zeta} K'_{\tau}(\beta_{\zeta} R_1)}{K_{\tau}(\beta_{\zeta} R)}, & \zeta \neq 0 \end{cases} \quad (A.2)$$

$$518 \quad L_{l,\zeta} = \int_{-h}^{-d} \cos[\beta_l(z+h)] Z_{\zeta}(z) dz = \begin{cases} \frac{(-1)^l (h-d)^2 k_0 Z_0(0) \sinh[k_0(h-d)]}{[(h-d)^2 k_0^2 + l^2 \pi^2] \cosh(k_0 h)}, & \zeta = 0 \\ \frac{(-1)^l (h-d)^2 k_{\zeta} Z_{\zeta}(0) \sin[k_{\zeta}(h-d)]}{[(h-d)^2 k_{\zeta}^2 - l^2 \pi^2] \cos(k_{\zeta} h)}, & \zeta \neq 0 \end{cases} \quad (A.3)$$

519 After inserting Eqs. (22) and (25) into Eq.(30), multiplying both sides by $Z_{\zeta}(z)\cos(\tau\theta)$ and
520 integrating for $z \in [-h,0]$ and $\theta \in [0,\pi]$, for any pair of integer (τ, ζ) , we have

$$521 \quad \sum_{l=0}^{\infty} \left(X_{\tau,l}^{(2)} C_{\tau,l}^{\chi} + Y_{\tau,l}^{(2)} D_{\tau,l}^{\chi} \right) L_{l,\zeta} - h Z_{\tau,\zeta}^{(2)} E_{\tau,\zeta}^{\chi} = f_2^{\chi}, \quad (A.4)$$

522 in which

$$523 \quad f_2^{\chi} = \begin{cases} -\frac{2\delta_{\zeta,0} \text{ig} A k_0 h}{\omega Z_0(0)} \varepsilon_{\tau} (-i)^{\tau} J'_{\tau}(k_0 R) \cos(\tau\beta), & \chi = S \\ 0, & \chi = R \end{cases}, \quad (A.5)$$

$$524 \quad X_{\tau,\zeta}^{(2)} = \begin{cases} \frac{\tau}{R}, & \zeta = 0 \\ \frac{\beta_{\zeta} I'_{\tau}(\beta_{\zeta} R)}{I_{\tau}(\beta_{\zeta} R)}, & \zeta \neq 0 \end{cases}; \quad Y_{\tau,\zeta}^{(2)} = \begin{cases} \frac{1}{R}, & \zeta = 0, \tau = 0 \\ -\frac{\tau}{R}, & \zeta = 0, \tau \neq 0, \\ \frac{\beta_{\zeta} K'_{\tau}(\beta_{\zeta} R)}{K_{\tau}(\beta_{\zeta} R)}, & \zeta \neq 0 \end{cases} \quad (A.6)$$

$$525 \quad Z_{\tau,\zeta}^{(2)} = \begin{cases} \frac{k_0 H'_\tau(k_0 R)}{H_\tau(k_0 R)}, & \zeta = 0 \\ \frac{k_\zeta K'_\tau(k_\zeta R)}{K_\tau(k_\zeta R)}, & \zeta = 1, 2, 3, \dots \end{cases} \quad (A.7)$$

526 After inserting Eqs. (16) and (22) into Eq.(31), multiplying both sides by $\cos[\beta_\zeta(z+h)]\cos(\tau\theta)$
 527 and integrating for $z \in [-h, -d]$ and $\theta \in [0, \pi]$, for any pair of integer (τ, ζ) , it can be obtained that

$$528 \quad \sum_{l=0}^{\infty} \left(\frac{\pi}{2} \left(\frac{\tilde{I}_\tau(k_l R_i)}{k_l \tilde{I}'_\tau(k_l R_i)} A_{\tau,l}^\chi + \frac{\tilde{I}_{-\tau}(k_l R_i)}{k_l \tilde{I}'_{-\tau}(k_l R_i)} A_{-\tau,l}^\chi \right) - i \sum_{\substack{m=-\infty \\ m \neq \pm \tau}}^{\infty} \frac{m \left[(-1)^{m-\tau} - 1 \right]}{m^2 - \tau^2} \frac{\tilde{I}_m(k_l R_i)}{k_l \tilde{I}'_m(k_l R_i)} A_{m,l}^\chi \right) L_{\zeta,l}^\chi, \\ = \frac{\pi(h-d)}{\varepsilon_\tau \varepsilon_\zeta} \left(X_{\tau,\zeta}^{(3)} C_{\tau,\zeta}^\chi + Y_{\tau,\zeta}^{(3)} D_{\tau,\zeta}^\chi \right) + f_3^\chi$$

$$529 \quad (A.8)$$

530 where

$$531 \quad f_3^\chi = \begin{cases} 0, & \chi = S \\ \frac{\delta_{\tau,0} \delta_{\zeta,0} i \pi (h-d)}{\rho \omega}, & \chi = R \end{cases}, \quad (A.9)$$

$$532 \quad X_{m,l}^{(3)} = \begin{cases} \left(\frac{R_i}{R} \right)^m, & l = 0 \\ \frac{I_m(\beta_l R_i)}{I_m(\beta_l R)}, & l \neq 0 \end{cases}; \quad Y_{m,l}^{(3)} = \begin{cases} 1 + \ln \left(\frac{R_i}{R} \right), & l = 0, m = 0 \\ \left(\frac{R}{R_i} \right)^m, & l = 0, m \neq 0 \\ \frac{K_m(\beta_l R_i)}{K_m(\beta_l R)}, & l \neq 0 \end{cases} \quad (A.10)$$

533 After inserting Eqs. (22) and (25) into Eq.(32), multiplying both sides by $\cos[\beta_\zeta(z+h)]\cos(\tau\theta)$
 534 and integrating for $z \in [-h, -d]$ and $\theta \in [0, \pi]$, for any pair of integer (τ, ζ) , we have

$$535 \quad \frac{h-d}{\varepsilon_\zeta} \left(C_{\tau,\zeta}^\chi + D_{\tau,\zeta}^\chi \right) - \sum_{l=0}^{\infty} E_{\tau,l}^\chi L_{\zeta,l}^\chi = f_4^\chi, \quad (A.11)$$

536 where

$$537 \quad f_4^\chi = \begin{cases} -\frac{2\varepsilon_\tau \text{ig} A L_{\zeta,0}}{\omega Z_0(0)} (-i)^\tau J_\tau(k_0 R) \cos(\tau\beta), & \chi = S \\ 0, & \chi = R \end{cases} \quad (A.12)$$

538 Eqs.(A.1), (A.4), (A.8) and (A.11) form a linear algebraic system, which can be used to solve

539 $A_{m,l}^\chi$, $C_{m,l}^\chi$, $D_{m,l}^\chi$ and $E_{m,l}^\chi$ numerically after truncation. In the present model, the infinite

540 terms of $e^{-im\theta}/\cos(m\theta)$, and $Z_l(z)/\cos[\beta_l(z+h)]$ are truncated at $m=M$ and $l=L$, respectively. Accurate

541 results can be obtained by choosing $M=12$, $L=20$.

542

References

- [1] Fleming AN, Macfarlane GJ. Experimental flow field comparison for a series of scale model oscillating water column wave energy converters. *Mar Struct.* 2017;52:108-25.
- [2] Sheng W, Alcorn R, Lewis A. Assessment of primary energy conversions of oscillating water columns. I. Hydrodynamic analysis. *J Renew Sustain Ener.* 2014;6:053113.
- [3] Guo B, Patton R, Jin S, Gilbert J, Parsons D. Nonlinear modeling and verification of a heaving point absorber for wave energy conversion. *IEEE T Sustain Ener.* 2018;9:453-61.
- [4] Zheng S, Zhang Y. Analysis for wave power capture capacity of two interconnected floats in regular waves. *J Fluid Struct.* 2017;75:158-73.
- [5] Renzi E, Dias F. Hydrodynamics of the oscillating wave surge converter in the open ocean. *European Journal of Mechanics B/Fluids.* 2013;41:1-10.
- [6] Fernandez H, Iglesias G, Carballo R, Castro A, Fraguera JA, Taveira-Pinto F, et al. The new wave energy converter WaveCat: Concept and laboratory tests. *Mar Struct.* 2012;29:58-70.
- [7] Drew B, Plummer AR, Sahinkaya MN. A review of wave energy converter technology. *P I Mech Eng a-J Pow.* 2009;223:887-902.
- [8] Falnes J. A review of wave-energy extraction. *Mar Struct.* 2007;20:185-201.
- [9] Mustapa MA, Yaakob OB, Ahmed YM, Rheem CK, Koh KK, Adnan FA. Wave energy device and breakwater integration: A review. *Renew Sust Ener Rev.* 2017;77:43-58.
- [10] Astariz S, Iglesias G. The economics of wave energy: A review. *Renew Sust Ener Rev.* 2015;45:397-408.
- [11] Heras-Saizarbitoria I, Zamanillo I, Laskurain I. Social acceptance of ocean wave energy: A case study of an OWC shoreline plant. *Renew Sust Ener Rev.* 2013;27:515-24.
- [12] Ning DZ, Zhao XL, Chen LF, Zhao M. Hydrodynamic performance of an array of wave energy converters integrated with a pontoon-type breakwater. *Energies.* 2018;11:685.
- [13] Perez-Collazo C, Greaves D, Iglesias G. Hydrodynamic response of the WEC sub-system of a novel hybrid wind-wave energy converter. *Energy Conversion and Management.* 2018;171:307-25.
- [14] Malara G, Gomes RPF, Arena F, Henriques JCC, Gato LMC, Falcão AFO. The influence of three-dimensional effects on the performance of U-type oscillating water column wave energy harvesters. *Renew Energ.* 2017;111:506-22.
- [15] Evans DV, Porter R. Hydrodynamic characteristics of an oscillating water column device. *Appl Ocean Res.* 1995;17:155-64.
- [16] Morris-Thomas MT, Irvin RJ, Thiagarajan KP. An investigation into the hydrodynamic efficiency of an oscillating water column. *Journal of Offshore Mechanics and Arctic Engineering.* 2007;129:273-8.
- [17] Elhanafi A, Fleming A, Macfarlane G, Leong Z. Underwater geometrical impact on the hydrodynamic performance of an offshore oscillating water column-wave energy converter. *Renew Energ.* 2017;105:209-31.
- [18] Sheng W, Alcorn R, Lewis A. Assessment of primary energy conversions of oscillating water columns. II. Power take-off and validations. *J Renew Sustain Ener.* 2014;6:053114.
- [19] López I, Iglesias G. Efficiency of OWC wave energy converters: A virtual laboratory. *Appl Ocean Res.* 2014;44:63-70.
- [20] López I, Pereiras B, Castro F, Iglesias G. Performance of OWC wave energy converters: influence of turbine damping and tidal variability. *Int J Ener Res.* 2015;39:472-83.
- [21] Pereiras B, López I, Castro F, Iglesias G. Non-dimensional analysis for matching an impulse turbine to an OWC (oscillating water column) with an optimum energy transfer. *Energy.* 2015;87:481-9.

- [22] Elhanafi A, Fleming A, Macfarlane G, Leong Z. Numerical energy balance analysis for an onshore oscillating water column-wave energy converter. *Energy*. 2016;116:539-57.
- [23] Malara G, Arena F. Analytical modelling of an U-Oscillating Water Column and performance in random waves. *Renew Energ*. 2013;60:116-26.
- [24] Malara G, Romolo A, Fiamma V, Arena F. On the modelling of water column oscillations in U-OWC energy harvesters. *Renew Energ*. 2017;101:964-72.
- [25] Ning D, Wang R, Zhang C. Numerical simulation of a dual-chamber oscillating water column wave energy converter. *Sustainability*. 2017;9.
- [26] He F, Huang Z, Law AWK. An experimental study of a floating breakwater with asymmetric pneumatic chambers for wave energy extraction. *Applied Energy*. 2013;106:222-31.
- [27] He F, Leng J, Zhao XZ. An experimental investigation into the wave power extraction of a floating box-type breakwater with dual pneumatic chambers. *Appl Ocean Res*. 2017;67:21-30.
- [28] Howe D, Nader JR. OWC WEC integrated within a breakwater versus isolated: Experimental and numerical theoretical study. *International Journal of Marine Energy*. 2017;20:165-82.
- [29] Falcão AFO, Henriques JCC, Gato LMC. Air turbine optimization for a bottom-standing oscillating-water-column wave energy converter. *Journal of Ocean Engineering and Marine Energy*. 2016;2:459-72.
- [30] Nader JR. Interaction of ocean waves with oscillating water column wave energy convertors. Wollongong: University of Wollongong; 2013.
- [31] Martins-rivas H, Mei CC. Wave power extraction from an oscillating water column at the tip of a breakwater. *J Fluid Mech*. 2009;626:395-414.
- [32] Martins-rivas H, Mei CC. Wave power extraction from an oscillating water column along a straight coast. *Ocean Eng*. 2009;36:426-33.
- [33] Lovas S, Mei CC, Liu YM. Oscillating water column at a coastal corner for wave power extraction. *Appl Ocean Res*. 2010;32:267-83.
- [34] Sarmiento AJNA, Falcão AFdO. Wave Generation by an Oscillating Surface-Pressure and Its Application in Wave-Energy Extraction. *J Fluid Mech*. 1985;150:467-85.
- [35] Zheng S, Zhang Y, Iglesias G. Wave-structure interaction in hybrid wave farms. *J Fluid Struct*. 2018;83:386-412.
- [36] Zheng S, Zhang Y. Theoretical modelling of a new hybrid wave energy converter in regular waves. *Renew Energ*. 2018;128A:125-41.
- [37] Zheng S, Zhang Y. Wave diffraction from a truncated cylinder in front of a vertical wall. *Ocean Eng*. 2015;104:329-43.
- [38] Zheng S, Zhang Y. Wave radiation from a truncated cylinder in front of a vertical wall. *Ocean Eng*. 2016;111:602-14.
- [39] Falnes J. Ocean waves and oscillating systems: Linear interaction including wave-energy extraction. Cambridge, UK: Cambridge University Press; 2002.